

Acoustically driven degradation in single crystalline silicon solar cell

O.Ya. Olikh

Faculty of Physics, Taras Shevchenko National University of Kyiv, Kyiv 01601, Ukraine

Abstract

The influence of ultrasound on current–voltage characteristics of crystalline silicon solar cell was investigated experimentally. The transverse and longitudinal acoustic waves were used over a temperature range of 290–340 K. It was found that the ultrasound loading leads to the reversible decrease in the photogenerated current, open–circuit voltage, fill factor, carrier lifetime, and shunt resistance as well as the increase in the ideality factor. The experimental results were described by using the models of coupled defect level recombination, Shockley–Read–Hall recombination, and dislocation–induced impedance. The contribution of the boron–oxygen related defects, iron–boron pairs, and oxide precipitates to both the carrier recombination and acousto–defect interaction was discussed. The experimentally observed phenomena are associated with the increase in the distance between coupled defects as well as the extension of the carrier capture coefficient of complex point defects and dislocations.

Keywords: silicon, solar cells, ultrasound influence

1. Introduction

The silicon solar cells (SSCs) are still dominant in the photovoltaic field due to their high efficiency, low selling price and process maturity. The material properties driving is a top priority for most of manufacturers of SSC or another semiconductor devices. For example, the loss in the SSC efficiency is observed due to illumination (the light–induced degradation or LID in the c–Si case [1–4] and the carrier-induced degradation or CID in the mc–Si case [5, 6]), high voltage (the potential–induced degradation or PID [7–9]), or irradiation (the radiation–induced degradation or RID [10, 11]). The degradation reason is a changing of crystal defects. That is a transformation of the boron–oxygen or copper–contained complex (in LID case), a decoration of the stacking faults by the positive ions, predominantly sodium, (in PID case) or a creation of the radiation recombination centers (RID case). The annealing at an elevated temperature is quite often required for efficiency recovery.

Email address: olikh@univ.kiev.ua (O.Ya. Olikh)

At the same time, the ultrasound (US) can effectively interact with defects in silicon. It was experimentally observed that US can cause transformation of impurity and radiation defects [12–17], modification of spectrum [18] and density [19] of surface states, changing of carrier diffusion length [20, 21], variation of current in barrier structures [22–27]. Hence, it is expected that ultrasound-induced degradation (USID) can be originated by the acoustic wave (AW) action. After AW propagation had stopped, the full recovery of material properties was often observed without annealing [12, 20–22]. Therefore, the USID is expected to be a reversible at room temperature in contrast to rest of degradations.

The aim of our work is to investigate experimentally the acoustically induced (AI) variation of crystalline SSC photo-electrical parameters. Ultrasound was found to result in a decrease in the solar cell efficiency. The US intensity did not exceed 0.5 W/cm^2 and the USID full recovery was observed at room temperature. The USID dependencies on the AW both type and intensity are presented. The experimentally observed phenomena are associated with the decrease in the carriers lifetime and in the shunt resistance as well as the increase in the ideality factor. To describe the processes in the space charge region (SCR) and in the diode base as well as to study shunt resistance, we used the models of coupled defect level recombination [28, 29], Shockley–Read–Hall (SRH) recombination and dislocation-induced impedance [30, 31], respectively. The observed AI phenomena are accounted for in terms of the defect interaction with the AW strain field [32, 33].

2. Experimental and calculation details

2.1. Samples

The SSC was fabricated from 2 in. ($300 \mu\text{m}$ thick) p-type boron doped Czochralski silicon wafer with $\langle 111 \rangle$ orientation and a doping level of $1.4 \times 10^{15} \text{ cm}^{-3}$. The n^+ emitter with a carrier concentration of about 10^{19} cm^{-3} and a thickness of $0.5 \mu\text{m}$ was formed by phosphorus implantation. The wafer surface was capped by the TiO_x antireflective coating. The front and rear aluminium electrodes were deposited by screen printing before rapid annealing.

The samples used in the experiment were cut from the wafer and mainly differed in the shunt resistance (R_{sh}) value. The typical results for the samples with low ($R_{sh} \simeq 10^4 \Omega \cdot \text{cm}^2$ at room temperature) and high ($R_{sh} > 10^{15} \Omega \cdot \text{cm}^2$) values are only presented in the article. These samples is labeled “SC4” and “SC15”, respectively, from now on.

2.2. Ultrasound loading

In case of ultrasound loading (UL), the transverse or longitudinal AWs, which were excited by using LiNbO_3 piezoelectric transducer, were applied to the samples at the base side in the $[111]$ -direction. The US frequencies f_{US} , intensities W_{US} , amplitudes of lattice deformation $\xi_{\text{US}} = \sqrt{2W_{\text{US}}/\rho_{\text{Si}} \vartheta_{\text{US}}^3}$, and lattice atom displacements $u_{\text{US}} = \sqrt{W_{\text{US}}/2\pi^2 f_{\text{US}}^2 \rho_{\text{Si}} \vartheta_{\text{US}}}$ are listed in Table 1.

Table 1: The ultrasound loading parameters.

f_{us} (MHz)	wave type	W_{us} (W/cm ²)	ξ_{us} (10 ⁻⁶)	u_{us} (nm)	UL label	subjected samples
8.0	longitudinal	0.18	1.3	0.3	lUL	SC4, SC15
4.2	transverse	0.19	2.8	0.6	tULa	SC15
4.2	transverse	0.22	3.1	0.7	tULb	SC4
4.2	transverse	0.40	4.2	0.9	tULc	SC4, SC15

$\rho_{Si} = 2.33 \text{ g/m}^3$ is the silicon density, v_{US} is the US velocity, 9850 m/s and 5840 m/s in cases of longitudinal and transverse AWs, respectively.

It was reported previously [13, 21, 27] that the characteristic time of change in silicon structure parameters under the US action did not exceed $2 \times 10^3 \text{ s}$. In order to wait until the AI transitional period is completed, the following experimental procedure was used. When USL started, the sample was first exposed to room temperature for 60 min and then the measurement and the sample heating were started. In order to avoid the effect of piezoelectric field on both the measurements and sample parameters, the transducer was shielded. The more details about the experimental setup are presented elsewhere [27].

2.3. Current-voltage measurements and SSC parameters determination

The dark and illuminated forward current-voltage (J - V) characteristics of the samples both with and without USL were measured over a temperature range of 290–340 K. The temperature was controlled by differential copper-constantan thermocouple. Some of the obtained curves are shown in Fig. 1.

The short-circuit current density J_{sc} , open-circuit voltage V_{oc} and the fill factor FF were estimated from the illuminated J - V curve by the conventional mode.

The double-diode model of n^+ - p SSC J - V characteristics is expressed in the following form:

$$J(V, T) = -J_{ph} + \frac{qn_i d}{2\tau_g} \left\{ \exp \left[\frac{q(V - JR_s)}{n_{id} kT} \right] - 1 \right\} + \frac{qn_i^2}{p_p} \sqrt{\frac{\mu_n kT}{\tau_n}} \left\{ \exp \left[\frac{q(V - JR_s)}{kT} \right] - 1 \right\} + \frac{V - JR_s}{R_{sh}}, \quad (1)$$

where J_{ph} is the photogenerated current density, n_i is the intrinsic carrier concentration, τ_g is the SCR carrier lifetime, d is the SCR thickness:

$$d(V, T) = \sqrt{\frac{2\varepsilon\varepsilon_0(p_p + n_n)}{qp_p n_n}} \left[\frac{E_g}{q} - \frac{kT}{q} \ln \left(\frac{N_v N_c}{p_p n_n} \right) - \frac{2kT}{q} - V \right], \quad (2)$$

ε is the permittivity (11.7 for Si), p_p and n_n are the majority carrier concentration in the p - and n -type regions, E_g is the semiconductor band gap, N_c and N_v are the effective density of states in the conduction and valence bands; n_{id} is the

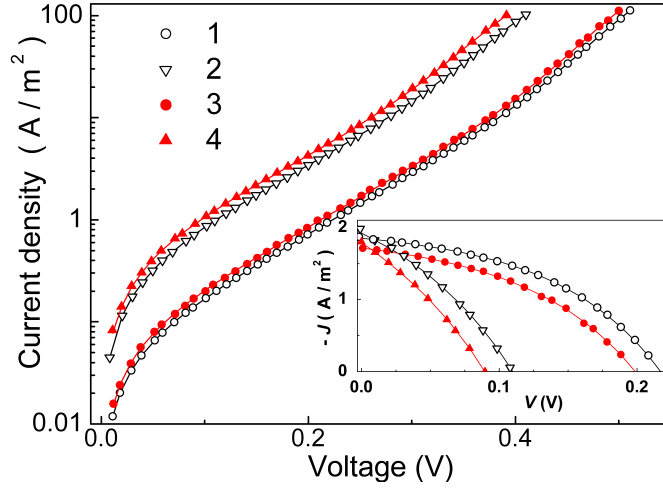


Figure 1: Dark J - V characteristics measured at 301 K (curves 1, 3, circles) and 341 K (curves 2, 4, triangles) with (2, 4, filled marks, tULc) and without (1, 3, open marks) UL. Inset: Parts of illuminated J - V characteristics over a voltage range of $0-V_{oc}$. The marks are the experimental results, and the lines are the curves fitted by Eqs. (1)–(2).

ideality factor, R_s is the series resistances, and μ_n and τ_n are the mobility and lifetime of the electron (minority carrier) in the diode base. The current-voltage equation that models the solar cell by an equivalent electrical circuit contains several parameters related to physical phenomena occurring in the device. It is commonly believed that $J_{0base} = (qn_i^2/n_n)\sqrt{\mu_n kT/\tau_n}$ is closely related to the recombination in the quasi-neutral region, while $J_{0SCR} = (qdn_i/2\tau_g)$ describes the overall SCR recombination.

We used Eqs. (1)–(2) to fit the experimental data taking τ_g , τ_n , n_{id} , R_{sh} , R_s , and J_{ph} (for illuminated J - V curves only) as the fitting parameters. Also, we used the known [34–36] temperature dependences of n_i , E_g , and μ_n . As a result, we obtained extremely good fit to the experimental data — see Fig. 1. The parameters values, obtained from the dark and illuminated measurement at the same temperature and UL option, were identical practically.

It is known that $J_{sc} \approx J_{ph}R_{sh}/(R_{sh} + R_s)$. The value of R_s was found to be about $2 \Omega \cdot \text{cm}^2$, whereas R_{sh} exceeded $4 \text{ k}\Omega \cdot \text{cm}^2$. Therefore it is expected that $J_{sc} \approx J_{ph}$. In fact, this relation was observed for the J_{ph} , which was obtained by fitting of whole of J - V curve, and the J_{sc} , which was obtained as a point of intersection of a J - V curve with a current axis.

To evaluate the US influence the relative change of parameters were used: $\varepsilon_P = (P_{in} - P_{us})/P_{in}$, where P is one of the set $\{J_{sc}, V_{oc}, FF, \tau_g, \tau_n, R_{sh}\}$, subscripts “US” and “in” indicate the values obtained at the same temperature with and without UL, respectively. The AI change of the ideality factor was characterized by the absolute value $\Delta n_{id} = n_{id,in} - n_{id,us}$.

2.4. Illumination

The monochromatic ($\lambda = 900$ nm) and low-intensity light was used for the SSCs illumination. It is known [37] that illumination with intensity of above 0.01 suns can lead to defect formation in p-type silicon. Our work was devoted to investigation of AI effects and the light intensity of $W_{ph} = (8 \pm 4)$ W/m² was chosen to avoid any current induced degradation processes. The light monochromatism allowed to simplify the short-current dependence. In case of used wavelength, the photocurrent defined by the electron-hole pairs generation in the *p*-region mainly. If the base is several minority carrier diffusion lengths $L_n = \sqrt{\mu_n k T \tau_n / q}$, the J_{sc} can be written as [36, 38]

$$J_{sc} = \frac{W_{ph}(1 - M)q\beta\lambda}{hc} \frac{\alpha L_n}{1 + \alpha L_n}, \quad (3)$$

where α is the absorption coefficient, M is the reflection coefficient, β is the quantum yield coefficient. We used Eq. (3) to fit the experimental $J_{sc}(T)$ data taking L_n as the fitting parameter. Also, we used the known [36] temperature dependence of α and supposed that β and M were temperature independent, $L_n \propto T^{0.5}$. The last relation was obtained from J - V curves fitting — see Sec. 3.3. Thus, L_n and τ_n can be obtained from the both single J - V curve and J_{sc} temperature dependence. To separate the second case values, the subscript “*ph*” was used: L_n^{ph} , τ_n^{ph} , $\varepsilon_{\tau_n}^{ph}$ etc.

2.5. Fitting procedure

All non-linear fittings were done by using the differential evolution method [39–41]. The least-squares method was used to linear fitting.

3. Results and Discussion

3.1. Photo-electric conversion

The obtained temperature dependences of the the short-circuit current density, open-circuit voltage and the fill factor are shown in Fig. 2. The parameters values at 320 K are listed in Tab. 2. It should be noted that not only I_{sc} and V_{oc} but also SSC efficiency, FF , and minority carrier lifetime decreases under low-intensity light conditions [42–44]. Hence, data in Fig. 2 and Table 2 are not equivalent to the standard test condition (AM1.5, 25°C, 1000 W/m²) results, but illustrate the AI effects.

Fig. 2 shows an acoustically driven degradation of the short-circuit current, open-circuit voltage, and fill factor. The parameters relative changes are listed in Table 3. We would like to stress that, firstly, all found AI effects are reversible. In other word, the J_{sc} , V_{oc} , FF , and another parameters, which are described above, revert to the initial value after the UL termination and sample storage for about 24 h at room temperature. The reversibility testifies that ultrasound neither causes defect diffusion nor changes defect concentration. Secondly, the AI relative changes are weakly depend on temperature over the explored range.

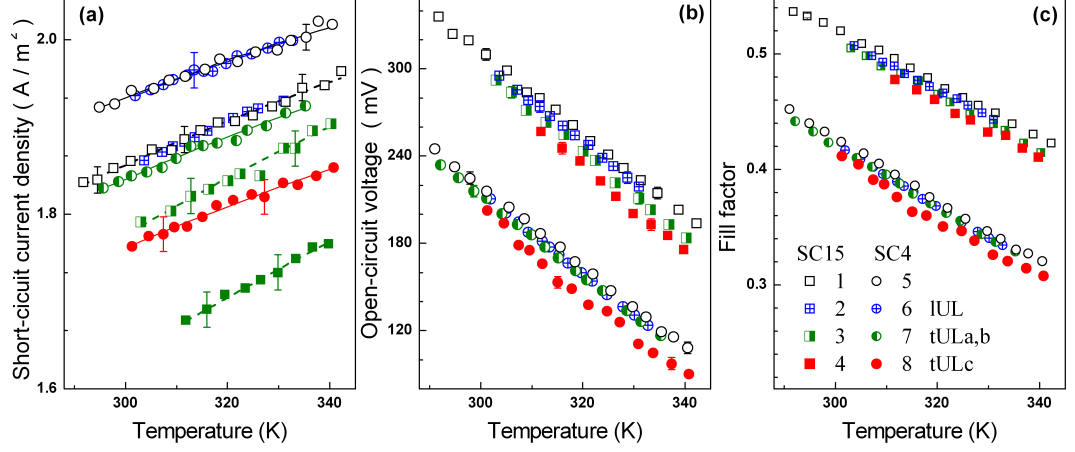


Figure 2: Temperature dependences of short-circuit (a), open-circuit voltage (b) and fill factor (c) for SC15 (squares) and SC4 (circles). The curves 1 and 5 (open marks) are obtained without UL, curves 2 and 6 correspond to IUL, curve 3 corresponds to tULa, curve 7 corresponds to tULb, curves 4 and 8 correspond to tULc. The marks are the experimental results, and the lines are the curves fitted by Eq. (3).

Table 2: The determined SSC parameters (at 320 K).

Parameter	SC15				SC4			
	non	Ultrasound loading			non	Ultrasound loading		
		IUL	tULa	tULc		IUL	tULb	tULc
J_{sc} ($0.01A/m^2$)	191 ± 2	191 ± 2	184 ± 2	171 ± 2	198 ± 2	198 ± 2	189 ± 2	181 ± 2
V_{oc} (mV)	256 ± 4	250 ± 4	243 ± 4	233 ± 4	164 ± 4	159 ± 4	157 ± 4	141 ± 4
FF (10^{-3})	475 ± 2	468 ± 2	463 ± 2	458 ± 2	372 ± 2	366 ± 2	366 ± 2	353 ± 2
L_n^{ph} (μm)*	99 ± 5	92 ± 5	67 ± 4	55 ± 3	125 ± 6	124 ± 6	103 ± 5	98 ± 5
L_n (μm)	88 ± 5	82 ± 4	47 ± 3	34 ± 2	106 ± 5	99 ± 5	80 ± 4	69 ± 4
τ_n^{ph} (10^{-7} s)*	31 ± 3	26 ± 3	14 ± 2	9 ± 1	49 ± 5	48 ± 5	33 ± 4	30 ± 3
τ_n (10^{-7} s)	24 ± 3	21 ± 3	7 ± 2	3.5 ± 0.7	35 ± 3	31 ± 3	20 ± 3	15 ± 2
τ_g (10^{-9} s)	70 ± 4	66 ± 3	57 ± 3	48 ± 2	35 ± 2	31 ± 2	30 ± 2	29 ± 2
$E_{\tau g}$ (meV)*	242 ± 7	237 ± 5	234 ± 5	234 ± 5	246 ± 6	234 ± 5	241 ± 5	243 ± 5
n_{id} (±0.01)	2.59	2.60	2.61	2.63	2.51	2.52	2.54	2.54
T_{id} (K)*	226 ± 8	215 ± 10	243 ± 15	233 ± 15	327 ± 10	319 ± 15	308 ± 20	358 ± 25

* determined by using the whole temperature range

Table 3: The acoustically induced change of SSC parameters.

Parameter	SC15			SC4		
	lUL	tULa	tULc	lUL	tULb	tULc
$\varepsilon_{J_{sc}}$ (%)	0±1	4±1	10±1	0±1	5±1	9±1
$\varepsilon_{V_{oc}}$ (%)	2±2	5±2	9±2	3±2	4±2	14±2
ε_{FF} (%)	2±1	3±1	4±1	2±1	2±1	5±1
ε_{Ln}^{ph} (%)	7±7	32±7	44±7	1±7	18±7	22±7
ε_{Ln} (%)	7±6	47±6	61±6	6±6	25±6	35±6
$\varepsilon_{\tau n}^{ph}$ (%)	16±15	55±15	70±15	2±15	33±15	39±15
$\varepsilon_{\tau n}$ (%)	13±12	71±12	85±12	11±12	43±12	57±12
$\varepsilon_{\tau g}$ (%)	6±5	19±5	31±5	9±5	14±5	17±5
Δn_{id} (10^{-2})	1±1	2±1	4±1	1±1	3±1	3±1

The US intensities of lUL, tULa, and tULb are close. But it is shown by J_{sc} and V_{oc} data that the tULa,b result in more prominent AI parameter changes. At the same time, lUL and tULa,b differ in the both f_{us} and u_{us} (ξ_{us}). It was previously shown [23, 45] that US influence on the silicon structures should arose with the f_{us} increase. Therefore the efficiency of US action on the SSC is determined by the atom displacement (lattice deformation) mainly and the transverse AWs are more effective influence tool.

Eq. (3) show that J_{sc} strongly depends on a carrier diffusion length. The determined by fitting L_n^{ph} , calculated τ_n^{ph} values, and its changes are given in Tables 2 and 3. The fitting results are shown on Fig. 2(a) by curves. Thus the US effects the minority carrier lifetime.

Unfortunately the analytical expressions for V_{oc} and FF are absent in the double-diode model case. But Eq. (1) show that the open-circuit voltage and fill factor depend on τ_n , n , τ_g , and R_{sh} . The next three Sections are devoted to the consideration of US influence on these parameters. The reasons of V_{oc} and FF change are discussed in Section 3.5.

3.2. Space charge region

The parameters of I - V characteristics associated with SCR phenomena are n_{id} and τ_g . The temperature dependences of the SCR carrier lifetime and ideality factor are shown in 3(a) and 3(b), respectively. The thermoactivated growth of SCR lifetime is observed over the explored temperature range — see 3(a). The measured temperature dependence of τ_g is well described by the following equation

$$\tau_g(T) = \tau_{g0} \exp\left(-\frac{E_{\tau g}}{kT}\right). \quad (4)$$

As shown in Fig. 3(b), the ideality factor decreases with the increase in temperature, and the dependence of n_{id} on $1/T$ is close to linear. Thus, dependence $n_{id}(T)$ can be expressed as

$$n_{id}(T) = n_{id,\infty} + T_{id}/T. \quad (5)$$

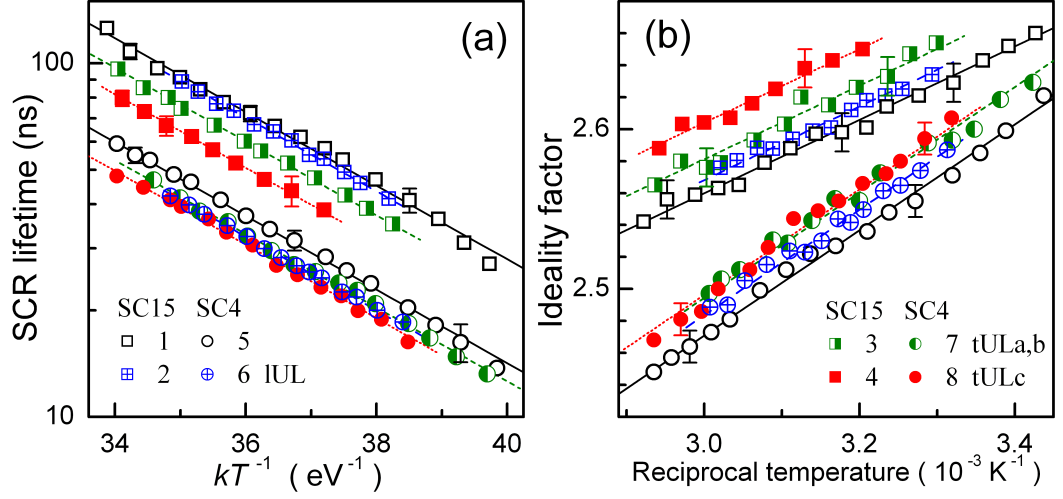


Figure 3: Temperature dependences of the SCR carrier lifetime (a) and ideality factor (b) for SC15 (squares, curves 1–4) and SC4 (circles, curves 5–8). The curves 1 and 5 (open marks) are obtained without UL, and curves 2 and 6 correspond to IUL, curve 3 corresponds to tULa, curve 7 corresponds to tULb, curves 4 and 8 correspond to tULc. The marks are the experimental results, and the lines are the fitted curves using Eq. (4) and $E_{\tau g} = 0.24$ eV (a) or Eq. (5) and $T_{id} = 330$ or 230 K (b).

The values of T_{id} and $E_{\tau g}$ found for samples under UL as well as without UL are listed in Table 2.

As seen from Fig. 3 and Table 2,

- (i) UL leads to the increase in n_{id} and decrease in τ_g ; the AI changes are listed in Table 3;
- (ii) τ_g and n_{id} are varied by tUL more effectively; $\varepsilon_{\tau g}$ and Δn_{id} increase with W_{US} enhancement;
- (iii) UL does not affect $E_{\tau g}$ and T_{id} values; $E_{\tau g}$ is equal to 0.24 ± 0.01 eV; T_{id} depends on sample and is equal to 330 ± 30 K (in the SC4 case) or 230 ± 20 K (in the SC15 case).

For the purpose of our analysis, it is important to discuss the recombination mechanism in SCR of the investigated samples. At first, the large n_{id} value and small τ_g value should be accentuated. According to classical SRH theory, the ideality factor must be smaller than 2, and τ_g temperature dependence is expected [46, 47] to be described by the relation

$$\tau_g \simeq 2 \tau_n \sqrt{\sigma_n / \sigma_p} \cosh[(E_t - E_i) / kT] \quad (6)$$

where σ_n , σ_p , and E_t are the electron and hole capture cross sections (CCSs) and the energy level of the recombination center, and E_i is the intrinsic energy

level. In our case, n_{id} is greater than 2, and τ_g increases with temperature. Therefore, SRH theory cannot be applied in our case.

Several attempts to account for large n_{id} value have been made by using different models. According to van der Heide *et al.* [48], the nonuniform contact resistance of the front side metallisation leads to a high n_{id} value. However, this theory predicts the dependence of ideality factor on light intensity, whereas n_{id} change with W_{ph} is not observed in our case. Beier and Voss [49] explain the large n_{id} by the saturation effects within the SRH-model. However, this theory is unable to explain the J_{0SCR} magnitude, which is much larger than expected for a silicon. The large ideality factor is attributed to the deep-level-assisted tunneling [50, 51] too. But according to this model, the n_{id} does not depend on temperature.

At the same time, all the observed features of SCR recombination can be explained by the model of coupled defect level recombination (CDLR) [28, 29, 52]. According to the CDLR model, the recombination is the result of carrier exchange between two defect levels and crystal bands. In particular, it is supposed [29] that the recombination rate is dominant at the sites where acceptor-like defect is coupled with donor-like defect. In a simplified case, when there is no carrier exchange between the donor level E_t^D and valence band, as well as between the acceptor level E_t^A and conduction band, the recombination rate R can be expressed [28] as

$$R = \frac{R_{12} - \sqrt{R_{12}^2 - 4\tau_n^D \tau_p^A (np - n_i^2)(1 - \epsilon)}}{2\tau_n^D \tau_p^A (1 - \epsilon)}, \quad (7)$$

$$R_{12} = \frac{(n + n_D)(p + p_A)}{R_{DA}} + \tau_n^D (p + p_D) + \tau_p^A (n + n_A), \quad (8)$$

$$\tau_n^D = (N_D \sigma_n^D v_{th,n})^{-1}, \quad \tau_p^A = (N_A \sigma_p^A v_{th,p})^{-1}, \quad (9)$$

where R_{DA} is the coupling parameter, N_D and N_A are the densities of donor and acceptor-like defects, σ_n^D and σ_p^A are the electron CCS of the donor and hole CCS of the acceptor, $v_{th,n}$ and $v_{th,p}$ are the thermal electron and hole velocities, $n_{D,A}$, $p_{D,A}$, and ϵ depend on E_t^D , E_t^A , and level degeneracy factors.

According to Steingrube *et al.* [29], CCS for defect in a pair differs from that for an isolated defect and depends on the distance r between the donor and the acceptor:

$$\sigma_{n,p}^{D,A}(r) \propto r^2, \quad (10)$$

R_{DA} is proportional to the overlap integral of the defect wave functions as well. If both defects are characterized by the H-like radial-symmetric wave function and equal Bohr radius a_0 , the following expression can be used: [29]

$$R_{DA}(r) \propto N_D N_A \left[1 + \frac{r}{a_0} + \frac{1}{3} \left(\frac{r}{a_0} \right)^2 \right] e^{-r/a_0}. \quad (11)$$

Unfortunately, the equation does not account for the functional relation between J - V characteristics parameters and attributes of defects taking part in

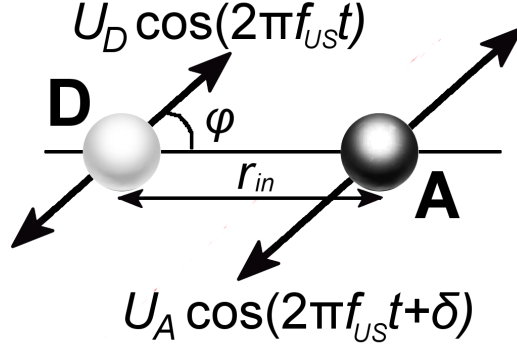


Figure 4: Model of CDLR center behavior under US action.

CDLR. However, it is shown [28, 52] that n_{id} increases with the decrement in R_{DA} . Since $\tau_g \propto R^{-1}$, the $n_{D,A}$, $p_{D,A}$, and ϵ are expected to provide a thermoactivated behavior of SCR lifetime. In our opinion, the value of E_{τ_g} is mainly determined by couple component energy levels, whereas the value of T_{id} is affected by N_D and N_A too. Hence, (i) same defects are take part in the SCR recombination in both SC15 and SC4 because the E_{τ_g} values are identical; (ii) the defect concentrations in SC15 and SC4 are different because the T_{id} , $\tau_{g,in}$, and $n_{id,in}$ values are different; (iii) UL does not result in the modification of the level position as well as defect concentration because the E_{τ_g} and T_{id} values are not affected.

In our opinion, the observed reversible AI modifications of n_{id} and τ_g are induced by donor–acceptor distance alteration in the samples under UL. In fact, according to the data [32, 33], the force acting on a point defect during UL can be expressed as

$$F_d = \chi \Delta\Omega_d \frac{\partial \xi(x, t)}{\partial x}, \quad (12)$$

where χ is the bulk elasticity modulus, $\Delta\Omega_d$ is the crystal volume change per defect (e.g. $\Delta\Omega_d < 0$ and $\Delta\Omega_d > 0$ for the vacancy and interstitial atom, respectively), ξ is the crystal lattice deformation, and AW propagates along x axis, $\partial \xi(x, t)/\partial x \propto \xi_{US}$. Therefore, a point defect vibrates under UL, so oscillation amplitude and phase are determined by both the defect character and AW intensity.

The simplest model, which is shown in Fig. 4, gives the following qualitative conclusion. Initially, the donor (D) and the acceptor (A) are separated by the distance r_{in} . Under UL, the defects would vibrate with amplitudes u_D and u_A . Depending on ξ_{US} , defect elastic strain ($\Delta\Omega_d^D$ and $\Delta\Omega_d^A$), and defect coupling the defect vibration amplitudes can have different values. The vibration axis coincides with AW displacement direction and forms angle φ with the line, which passes throw the defect initial positions. δ is the phase shift between donor and

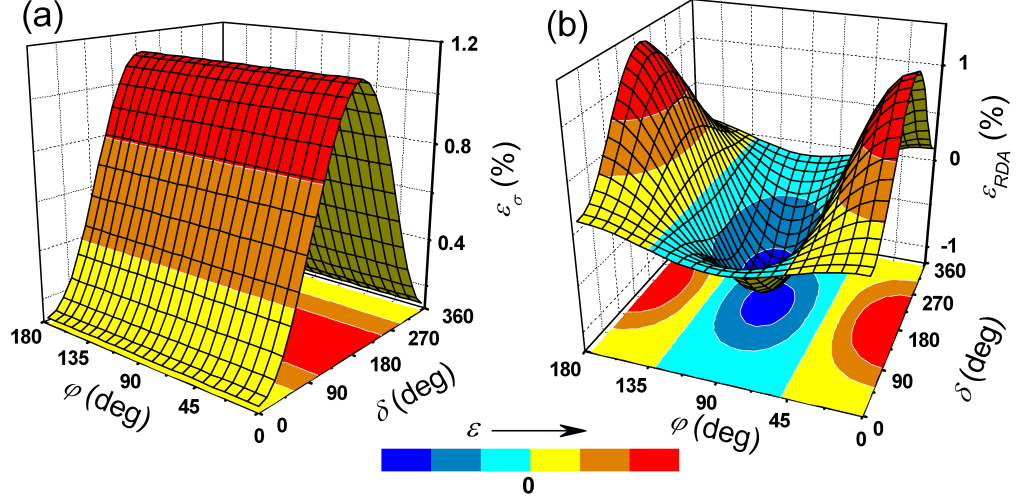


Figure 5: Simulated dependencies of AI changes of capture cross section (a) and coupling parameter (b) on the vibration phase shift and AW displacement direction. The parameters are set to $a_0 = 3.23$ nm, $r_{in} = 10$ nm, $u_A = 1$ nm, and $u_D = 0.5$ nm.

acceptor vibration.

We use Eqs. (10) and (11) to estimate AI relative changes of CCS $\varepsilon_\sigma = [\sigma_{US} - \sigma(r_{in})]/\sigma(r_{in})$ and coupling parameters $\varepsilon_{RDA} = [R_{DA,US} - R_{DA}(r_{in})]/R_{DA}(r_{in})$, where σ_{US} and $R_{DA,US}$ are averaged over the AW period. The results of simulation are shown in Figs. 5 and 6. In this estimation, the relaxation time in the CDLR sub-system is assumed to be considerably shorter than f_{US}^{-1} , and we apply the previously used [29] value $a_0 = 3.23$ nm. In addition, the chosen u_D and u_A values are commensurate with u_{US} . However, it should be taken into account that the displacement of the point defect without the covalent bond could exceed a matrix atom displacement.

Fig. 5(a) show that the UL leads to the increase in SSC. The AI alteration of coupling parameter is more complicated — see Fig. 5(b). In particular, the decrease in R_{DA} is expected in case of $\varphi \approx 90^\circ$ [the couple axis is perpendicular to the AW displacement direction, see Fig. 6(b)] or in case of low r_{in}/a_0 value [see Fig. 6(a)]. In the lat case, the intensive CDLR is expected [28, 29].

Thus, according to the our model estimation, UL causes the donor-acceptor distance change and results in ε_σ and ε_{RDA} , which mainly depend on lattice deformation. According to the CDLR theory, the increase in the SSC and decrease in the coupling parameters should lead to the decrease in the carrier lifetime and increase in the ideality factor. It was observed in the experiment.

3.3. Ultrasound influence on recombination in the SSC base

The L_n values, which are obtained from a recombination current in the quasi-neutral region (106 ± 10 μm and 88 ± 10 μm for SC-R4 and SC-R15 respectively

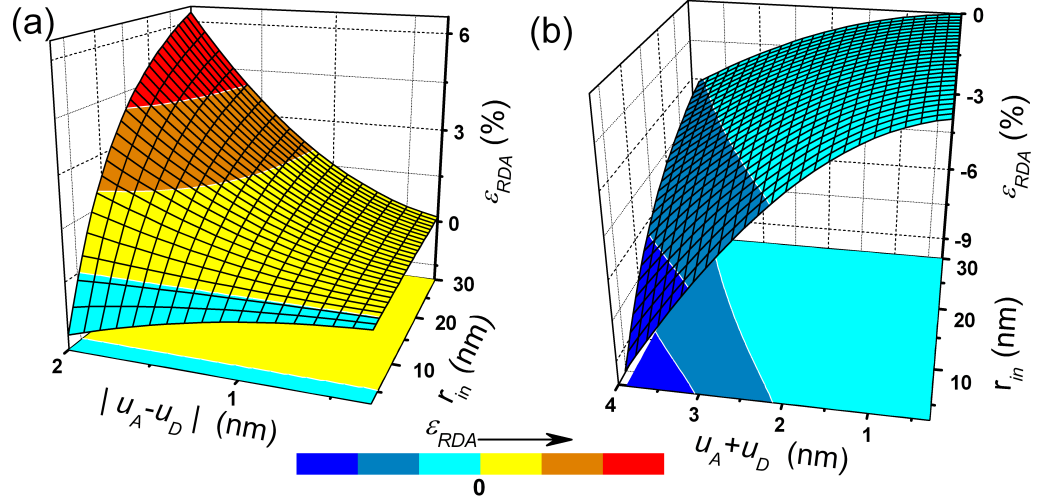


Figure 6: Simulated dependencies of AI changes of coupling parameter on the vibration amplitudes and initial donor-acceptor distance. The parameters are set to $\varphi = 0^\circ$, $\delta = 0^\circ$ (a), and $\varphi = 90^\circ$, $\delta = 180^\circ$ (b).

at 320 K without USL) and from a photocurrent temperature dependence ($125 \pm 15 \mu\text{m}$ and $99 \pm 15 \mu\text{m}$ for SC-R4 and SC-R15), are comparable. The relative changes of lifetime, obtained from J_{ph} , $\varepsilon_{\tau_n}^{J_{ph}}$ are listed in the Table 3. The values of $\varepsilon_{\tau_n}^{J_{ph}}$ and ε_{τ_n} agree qualitatively. The slight quantitative difference, which is observed in the T-USL case, can be dealt with the AI change of L_n temperature dependence probably.

Temperature dependencies of the minority carrier lifetime in the p-region of SSC are shown in Fig. 7. The SRH lifetime due a defect in p-type material at low injection level can be written as

$$\tau_n = (N_d \sigma_n \nu_{th})^{-1}, \quad (13)$$

where N_d is the concentration of the defect, ν_{th} is the thermal velocity. To our mind, the slight increment of τ_n with T results from the σ_n temperature dependency, which is mentioned above. As one can see, the USL causes the lifetime τ_n decrease, that runs down to 20% of τ_n initial value. The relative AI change of an electron lifetime ε_{τ_n} is presented in Table 3.

Finally, no US absorption by the defect is assumed. In this simple case, δ is equal to 0° if $(\Delta\Omega_d^p \cdot \Delta\Omega_d^A) > 0$ or to 180° if $(\Delta\Omega_d^p \cdot \Delta\Omega_d^A) < 0$. In addition, ε_{RDA} exclusively depends on $|u_D - u_A|$ (in the $\delta = 0^\circ$ case) or $|u_D + u_A|$ (in the $\delta = 180^\circ$ case). Moreover, these dependencies are identical in both cases. Relative changes of CCS depend on oscillation amplitudes with similar features and do not depend on φ :

$$\varepsilon_\sigma = (u_D \pm u_A)^2 / 2 r_{in}^2 = K_{US}^{DA} W_{US}, \quad (14)$$

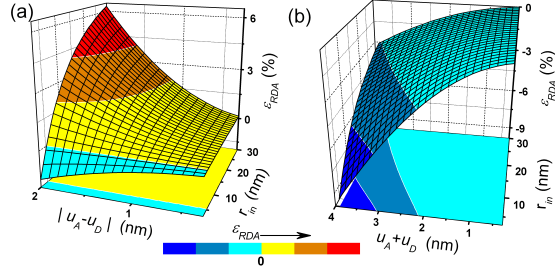


Figure 7: Temperature dependencies of base carrier lifetime for the SC-R15 (squares, 1–4) and SC-R4 (circles, 5–8) with (2–4 and 6–8) and without (1 and 5) USL. $W_{US}, W/cm^2$: 0.18 (2, 6), 0.19 (3), 0.22 (7), 0.40 (4, 8).

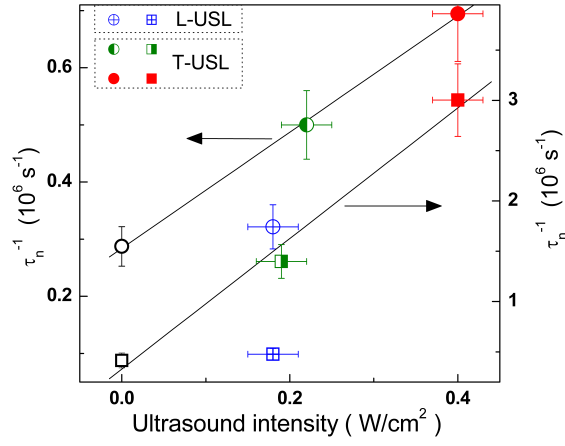


Figure 8: Dependencies of reciprocal lifetime in the SSC base on ultrasound intensity for the SC-R4 (circles, left axis) and SC-R15 (squares, right axis) at 320 K. Symbol filling is defined by the intensity and type of ultrasound waves and coincides with Fig. 7 notation. Lines are linear fitting of T-USL data.

where “+” and “−” correspond to $\delta = 180^\circ$ and $\delta = 0^\circ$, respectively, K_{US}^{DA} characterizes the defect couple–ultrasound interaction and depends on properties defects as well as crystal matrix. Equation (14) takes into account that $u_D, u_A \propto \xi_{US} \propto \sqrt{W_{US}}$.

Ordinary the lifetime reduction under radiation action is described by the Messenger-Spratt equation [36]:

$$\tau_n^{-1} = \tau_{n0}^{-1} + K\Phi, \quad (15)$$

where τ_{n0} is the minority carrier lifetime in the unirradiated cell, Φ is the integrated flux, and K is a lifetime damage constant characteristic for the material and the type of irradiation. The dependencies of reciprocal lifetime on ultrasound intensity are shown on Fig. 8. As one can recognize, the linear dependence of $1/\tau_n$ on W_{US} is observed. Therefore the modified Messenger-Spratt equation can be used to describe the acoustically driven change of the lifetime:

$$\tau_n^{-1} = \tau_{n0}^{-1} + K_{US}W_{US}, \quad (16)$$

where τ_{n0} is the lifetime in the ultrasound-free cell and K_{US} depends on a wave type and a sample state. The defined K_{US} values are listed in Table 2. Taking into account Eq. (13) and reversibility of ultrasound influence, we assume the observed decrement in lifetime to be evident of AI change of σ_n . In this case the following relation can be obtained by using Eqs. (13) and (16):

$$\frac{\varepsilon_\sigma}{\tau_{n0}W_{US}} = K_{US}. \quad (17)$$

The most recombination centers in the silicon are known to be a complex defect, which is composed of non-equivalent components. For example, the complexes of two point defects with an opposite charge occur quite often. Following the empirical relation proposed in [53], we believe, that the capture cross section of such pair depends on distance between complex’s component and Eq. (7) is true. Hence the introduced in Sec. 3.2 model of AI increase of σ is applicable to account for τ_n decrease. Really, according to the model $\varepsilon_\sigma \sim u_{D,A}^2 \sim \xi_{US}^2 \sim W_{US}$, i.e. the linear τ_n^{-1} – W_{US} relation is expected and is observed — see Fig. 8. The K_{US} increment in the T–USL and SC–R15 cases (Table 2) relates to the larger ξ_{US} – W_{US} proportionality coefficient and smaller τ_{n0} value respectively. It should be noted that an initial distance between components of recombination center is much smaller than the distance between participants of CDLR recombination; therefore according to Eq. (14), the more effective ultrasound influence is expected.

3.4. Ultrasound influence on shunt resistance

Fig. 9 illustrates R_{sh} modification for the sample under USL condition. One can see that the T–USL leads to moderate R_{sh} decrease whereas the L–USL does not change shunt resistance practically.

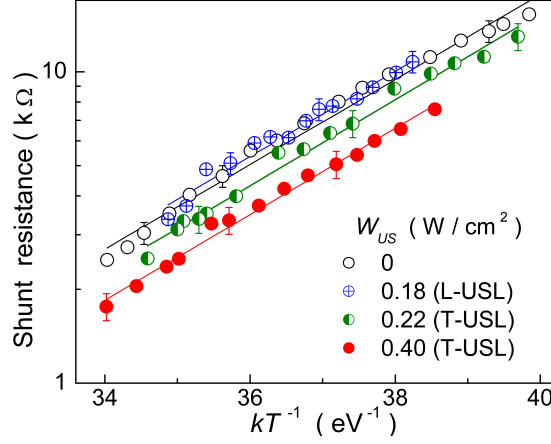


Figure 9: Plot of R_{sh} as the function of kT for the SC-R4 with and without USL. Lines are the fitted curves using Eq. (18)

Several non-mechanical reasons of SSC shunt resistance appearance are known [54]. They are aluminum particles, macroscopic Si_3N_4 inclusions, inversion layers at precipitates. During firing Al will alloy in, leading to a p^+ -doped region around the particle, which may compensate the emitter and may be in ohmic contact with the base. Subsequent annealing had to increase this p^+ -region and to decrease R_{sh} . Such behavior conflicts with data, which are presented on Sec. 3.6. Inversion layers and Si_3N_4 inclusions occur in multicrystalline silicon cells mainly [54] and cannot cause a shunt resistance of the investigated samples too. On the other hand, dislocations, which intersect the junction, are generally held responsible as a possible source of ohmic current [54–56]. Dislocations should be strongly recombinative, its recombination current may become strong enough for it to act as a shunt. For this reason they should be decorated by impurities [54].

Gopal and Gupta [30, 31] introduced the model of dislocation-induced impedance of photovoltaic detector. According to this model, the R_{sh} can be given by

$$R_{sh} = kT R_{dis} \cosh\left(\frac{E_{dis} - E_i + U_s}{2kT}\right) \cosh\left(\frac{E_{dis} - E_i - U_s}{2kT}\right), \quad (18)$$

with

$$R_{dis}^{-1} = \rho_{dis} A q^2 A_{dis} \sqrt{K_n K_p} N_{dis} (n_p + p_p), \quad (19)$$

where E_{dis} is the energy level which significantly contributes to the dislocation recombination current, E_i is the intrinsic Fermi level, U_s is the potential at the surface of the dislocation core, ρ_{dis} and A_{dis} are the dislocation density and surface area, respectively, K_n and K_p are the capture probabilities for electrons and holes by the dislocation states, N_{dis} is the density of surface states at each dislocation. Eq. (18) is reduced for the simplified case $K_p = K_n$. It should be

noted that a similar temperature dependence of a SSC shunt resistance is used elsewhere [57] too.

We use Eq. (18) to fit the experimental R_{sh} data. $(E_{dis} - E_i)$, U_s and R_{dis} are taken as the fitting parameters. It was established that the good agreement of the experimental data with the fitting curves has been observed (see Fig. 9) for values $(E_{dis} - E_i) = (0.34 \pm 0.02)$ eV and $U_s = (5 \pm 4) \times 10^{-8}$ eV, which were independent of USL. The obtained value $(E_{dis} - E_i)$ corresponds to the carrier activation energy $E_a \simeq 0.5E_g - (E_{dis} - E_i) \simeq 0.22$ eV, which is comparable to the values reported by other researcher. Thus activation energies $0.22 \div 0.25$ eV [58], 0.28 eV [59], 0.19 eV [60] and 0.23 eV [61] are associated with an impurity at the dislocation or with an intrinsic dislocation levels.

The R_{dis} value decreases in the T-USL case and its relative changes $\varepsilon_{R_{dis}}$ are shown in Table 3. On our opinion this is caused by an augmentation of A_{dis} in Eq. (19). The dislocation core atom displacement is parallel and normal to the current direction in the L-USL case and T-USL case respectively. As the result, in the T-USL case carriers are captured by dislocation levels from enlarged volume. It induces the effective surface area increase and the shunt resistance decrease.

3.5. Open-circuit voltage and fill factor simulation

To show V_{oc} and FF dependencies on τ_n , n_{id} , τ_g , and R_{sh} we have simulated J - V characteristics at different parameters value by using Eqs. (1) and (3). The values, that are close to investigated SSCs parameters, are used for simulation. The results are shown on Figures 10 and 11.

One can see on Figs. 10(a) and 11(a) that τ_g decrease should lead to a decrement of both V_{oc} and FF . At the same time the open-circuit voltage and the fill factor dependencies on τ_n are weak for the investigated SSC. Figures 10(b) and 11(b) show that the n_{id} as well as R_{sh} influence on V_{oc} and FF depends substantially on shunt resistance value. Thus if $R_{sh} > 10^5 \Omega$ (SC-R15 case) then V_{oc} increases with an ideality factor increment and both V_{oc} and FF don't depend on shunt resistance value practically. Whereas if $R_{sh} \leq 10^4 \Omega$ (SC-R4 case) then the open-circuit voltage and the fill factor decrease with shunt resistance decrement, but FF only depends on n_{id} weakly.

Thereby the discussed above AI decrease of τ_g leads to degradation of open-circuit voltage and the fill factor in the USL case. This effect is enhanced by AI R_{sh} decrease in the SC-R4 and is recovered partially by AI n_{id} increase in the SC-R15.

3.6. Light and annealing influence on the SSC parameters

Any concrete defect title was not referred as an recombination center in the discussion above. The additional investigations are necessary to define the type of defects, which are involved in both the recombination and the acousto-defect interaction.

It is known that the most harmful recombination centers in boron-doped Czochralski-grown SSC are the boron-oxygen related defects [2, 62–64], iron-boron pairs [62, 65, 66] (or another Fe-related trap in the n^+p -junctions [67,

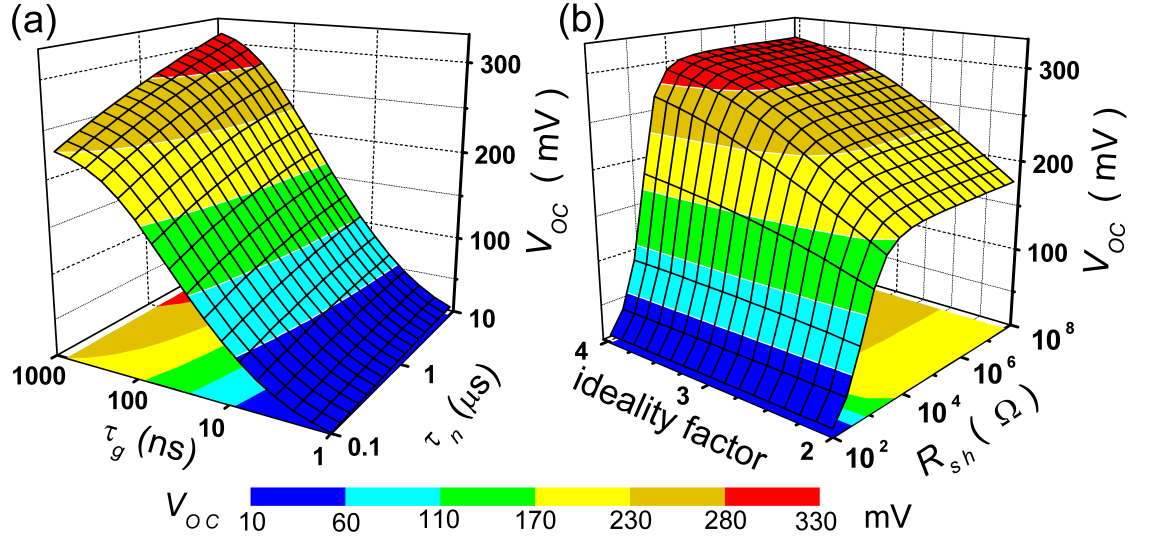


Figure 10: Simulated open-circuit voltage dependencies on SCR carrier lifetime and base carrier lifetime (a) and on ideality factor and shunt resistance (b). The constant values $n = 2.55$ (a), $R_{sh} = 5 \cdot 10^3 \Omega$ (a), $\tau_n = 3 \cdot 10^{-6} \text{ s}$ (b), $\tau_g = 5 \cdot 10^{-8} \text{ s}$ (b), and $T = 320 \text{ K}$ were used.

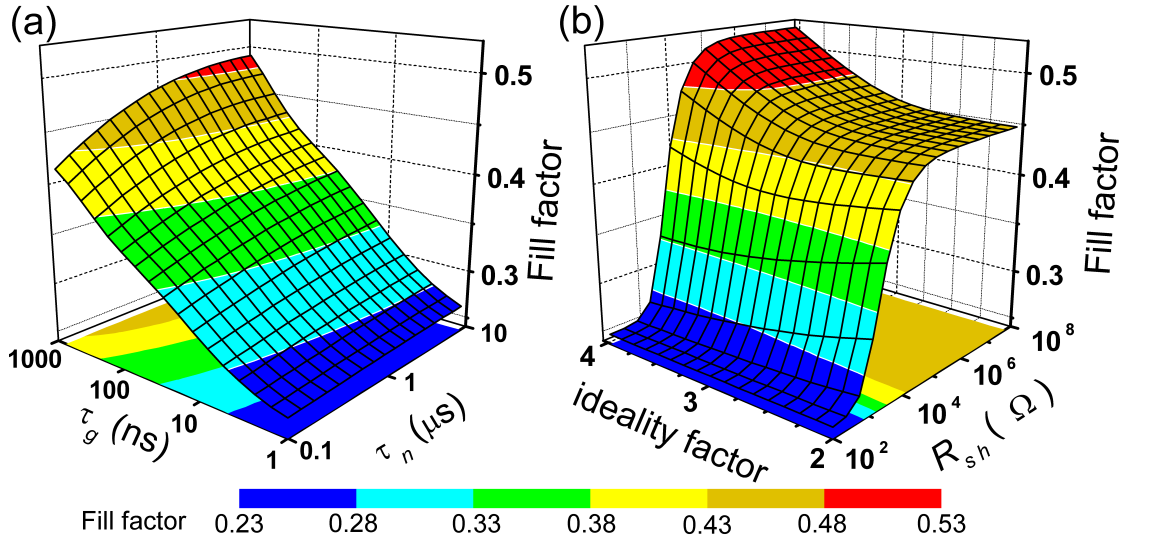


Figure 11: Simulated fill factor dependencies on SCR carrier lifetime and base carrier lifetime (a) and on ideality factor and shunt resistance (b). The constant values $n = 2.55$ (a), $R_{sh} = 5 \cdot 10^3 \Omega$ (a), $\tau_n = 3 \cdot 10^{-6} \text{ s}$ (b), $\tau_g = 5 \cdot 10^{-8} \text{ s}$ (b), and $T = 320 \text{ K}$ were used.

68]), and oxide precipitates [62, 69–72]. The first two defects are sensitive to an intensive illumination at room temperature. Thus transformation of boron–oxygen defects by an illumination leads to minority–carrier lifetime degradation (down to as 5 times as small [2]). Full lifetime recovery is observed after annealing at 200 °C for 10 min in the dark. The degradation–recovery cycle can be reiterated [63]. On the other hand, at room temperature, the vast majority of iron exists in iron–boron pairs, which can be readily dissociated under intense illumination to release interstitial iron. This gives a lifetime change which depends on doping concentration and excess carrier concentration [66]. After the dissociation procedure, the concentration of Fe_i decreases according to [62]

$$N_{Fe}(t) = (N_{Fe,0} - N_{Fe,eq}) \exp \left[-1.3 \cdot 10^{-3} p_p^{2/3} \exp \left(-\frac{0.68}{kT} \right) t \right] + N_{Fe,eq}, \quad (20)$$

where $N_{Fe,0}$ and $N_{Fe,eq}$ are the concentration after dissociation immediately and equilibrium concentration which remains a long time after dissociation respectively.

To inspect an availability of boron–oxygen defects and iron–boron pairs the following experimental procedure has been used. The samples were light soaked under halogen lamp (2 Suns) illumination at approximately 305 K. The illumination time varied from 1 h to 8 h. After illumination samples are stored in the dark at room temperature. To determine the kinetics of SSC parameters the dark J – V characteristics have been measured with interval 10–15 min at room temperature over a period 5 h after illumination stopping. To determine the permanent LID of SSC parameters the dark J – V characteristics have been measured in 48 h after illumination. After accumulated time under illumination had reached 10–15 h the samples were annealed at 200 °C for 10 min in the dark and SSC parameters were determined at room temperature. After that, the illumination–annealing cycle was repeated.

The results of residual influence of both illumination and annealing on an equilibrium value of SSC parameters are presented on Fig. 12. In contrast to other Figures, this contains sample SC–R3 data. The SC–R3 distinctive features are a low R_{sh} value and a performance of annealing before illumination. Though the obtained results for SC–R3 are similar to other samples. One can see that the illumination does not affect a SCR carrier lifetime as well as a base carrier lifetime neither before annealing, nor after. Illumination induced decrease of ideality factor is commensurable with an accuracy of n_{id} determination. Change of shunt resistance under illumination is most considerable but it reaches –20 % only and does not recur after an annealing – see Fig. 12(d), curve for the sample SC–R4. Annealing had more efficient influence on SSC parameters and results in an increment of τ_g and R_{sh} as well as in a decrement of τ_n and n_{id} . Such behavior of SSC parameters under illumination and annealing action is evident of absence of boron–oxygen defects influence. The reason of light induced and annealing induced changes will not be further discussed since this is beyond scope of our study.

The typical dependencies of SSC parameters versus time since illumination stopping are shown on Fig. 13. As one can see, τ_n and R_{sh} do not vary practically.

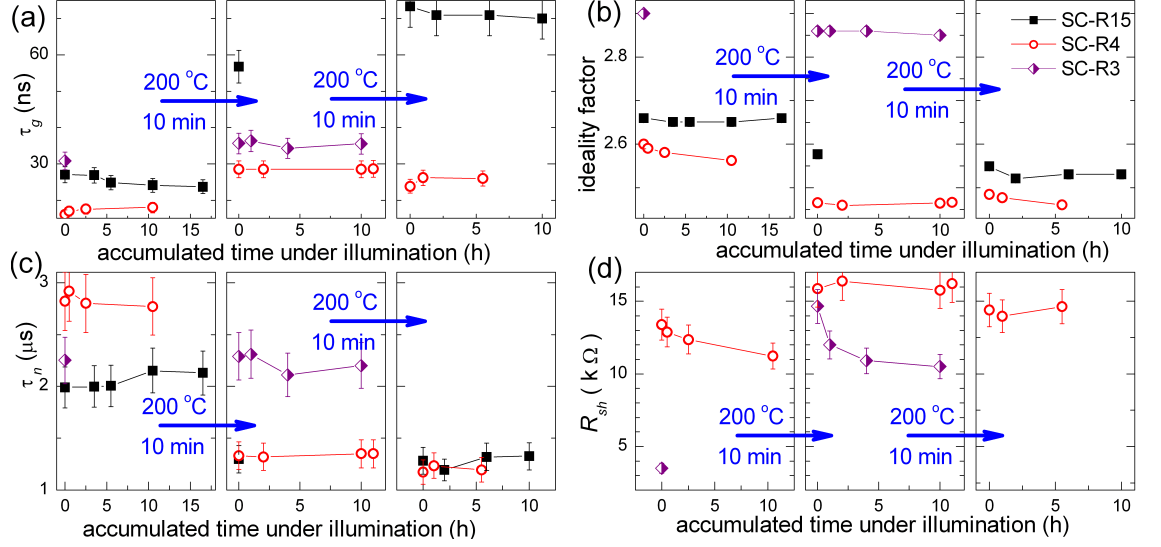


Figure 12: Dependencies of SCR carrier lifetime (a), ideality factor (b), base carrier lifetime (c), and shunt resistance (d) on accumulated illumination time and annealing. Data were obtained from J - V curves which had measured in 48 h after illumination or annealing at $T = 295$ K. Lines only serve as guide to the eye.

Hence these parameters can not be influenced by iron–boron pairs. At the same time τ_g and n_{id} are changing after illumination. We supposed that the expressions, that have described the both τ_g and n_{id} evolution, were similar to Eq. (20) and used the characteristic time $[1.3 \cdot 10^{-3} (1.4 \times 10^{15})^{2/3} \exp(-\frac{0.68}{295k})]^{-1} = 2.53 \cdot 10^4$ s to plot fitting line on Figs. 13(a) and (b). The fitting is in good agreement with experimental data. Therefore pairs Fe_iB_s can affect a SCR recombination and the acceptor level $E_C - 0.23$ eV can be involved in a CDLR recombination process. Incidentally, pair Fe_iB_s is a good candidate for acousto-active defect: the B is substitutional atom whose volume is smaller than the volume of the matrix atom and $\Delta\Omega_d(B_s) < 0$ whereas the interstitial Fe leads to $\Delta\Omega_d(Fe_i) > 0$. On the other hand, the τ_g change after illumination is about 10 % (see Fig. 13(a)), whereas a capture cross sections change, which is expected due to pair dissociation, equals to 1.7 times for electrons and 0.04 times for holes [66]. Hence, on our opinion, the pair Fe_iB_s is not main reason of a SCR recombination in the investigated samples.

According to Murphy *et al.* [69, 71], the recombination at oxide precipitates cannot be explained by a single two-level defect alone and at least two independent defects are exist. These defects have single energy levels at $E_V + 0.22$ eV and $E_C - 0.08$ eV and have $\sigma_n/\sigma_p = 157$ and $\sigma_p/\sigma_n = 1200$ respectively [71]. So, these defects are suitable for the CDLR recombination process. Dislocations and stacking faults surround the oxide precipitates and lead to capture coefficient change as well as to increase the concentrations of two defects, without

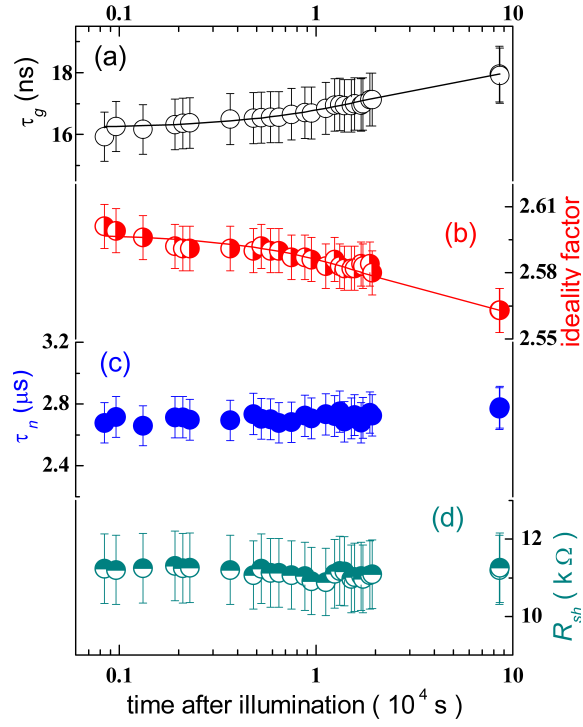


Figure 13: SCR carrier lifetime (a), ideality factor (b), base carrier lifetime (c), and shunt resistance (d) as a function of time since illumination stoping. Sample SC-R4. $T = 295$ K. Lines are plotted by using Eq. (20) and characteristic time $2.53 \cdot 10^4$ s.

introducing additional states into the bandgap [62, 69, 71] and can provide their acousto-activity. The oxide precipitates are nonuniformly distributed across a Cz-Si wafer [70] or a solar cell [72] and it is the probable reason for a SSC parameters variation from one investigated sample to another. On the basis of mentioned above, we conclude that the defects, involved in both recombination and acousto-defect interaction are oxide precipitates mainly.

4. Conclusion

The experimental investigation of ultrasound influence on the silicon solar cell has been carried out in the temperature range from 290 to 340 K. The investigation has revealed the acoustically driven reversible degradation of SSC parameters. It has been found out that the transverse ultrasound waves are more effective tools to affect silicon structure parameters than longitudinal ones. It has been given evidence that the degradation is due to the recombination amplification under the ultrasound wave action. The analysis has shown that the acoustically induced increase of carrier capture coefficient of point or extended defects is a reason of observed effects. The qualitative model of ultrasound influence, which is based on a change of a distance between defects or between components of defect complex under alternating deformation action, is proposed. It has been shown that the oxide precipitates are most likely defects, which take part in the acousto-defect interaction. Thus, ultrasound can be an effective tool for controlling silicon structure characteristics.

References

References

- [1] J. Schmidt, K. Bothe, D. Macdonald, J. Adey, R. Jones, D. Palmer, Electronically stimulated degradation of silicon solar cells, *Journal of Materials Research* 21 (1) (2006) 5–12. doi:10.1557/JMR.2006.0012.
- [2] J. Lindroos, H. Savin, Review of light-induced degradation in crystalline silicon solar cells, *Sol. Energy Mater. Sol. Cells* 147 (2016) 115–126. doi:http://dx.doi.org/10.1016/j.solmat.2015.11.047.
- [3] T. Niewelt, J. Schöon, W. Warta, S. W. Glunz, M. C. Schubert, Degradation of crystalline silicon due to boron-oxygen defects, *IEEE Journal of Photovoltaics* 7 (1) (2017) 383–398. doi:10.1109/JPHOTOV.2016.2614119.
- [4] H. Vahlman, A. Haarahiltunen, W. Kwapil, J. Schon, A. Inglese, H. Savin, Modeling of light-induced degradation due to Cu precipitation in p-type silicon. II. comparison of simulations and experiments, *J. Appl. Phys.* 121 (19) (2017) 195704. doi:10.1063/1.4983455.

- [5] C. Vargas, Y. Zhu, G. Coletti, C. Chan, D. Payne, M. Jensen, Z. Hameiri, Recombination parameters of lifetime-limiting carrier-induced defects in multicrystalline silicon for solar cells, *Appl. Phys. Lett.* 110 (9) (2017) 092106. doi:10.1063/1.4977906.
- [6] D. N. R. Payne, C. E. Chan, B. J. Hallam, B. Hoex, M. D. Abbott, S. R. Wenham, D. M. Bagnall, Acceleration and mitigation of carrier-induced degradation in p-type multi-crystalline silicon, *Phys. Status Solidi RRL* 10 (3) (2016) 237–241. doi:10.1002/pssr.201510437.
- [7] V. Naumann, D. Lausch, A. Hahnel, J. Bauer, O. Breitenstein, A. Graff, M. Werner, S. Swatek, S. Grober, J. Bagdahn, C. Hagendorf, Explanation of potential-induced degradation of the shunting type by Na decoration of stacking faults in Si solar cells, *Sol. Energy Mater. Sol. Cells* 120 (2014) 383–389. doi:10.1016/j.solmat.2013.06.015.
- [8] S. Hoffmann, M. Koehl, Effect of humidity and temperature on the potential-induced degradation, *Progress in Photovoltaics: Research and Applications* 22 (2) (2012) 173–179. doi:10.1002/pip.2238.
- [9] K. Hara, K. Ogawa, Y. Okabayashi, H. Matsuzaki, A. Masuda, Influence of surface structure of n-type single-crystalline Si solar cells on potential-induced deinfluence, *Sol. Energy Mater. Sol. Cells* 166 (2017) 132–139. doi:10.1016/j.solmat.2017.03.018.
- [10] S. Bhat, A. Rao, S. Krishnan, G. Sanjeev, S. E. Puthanveetil, A study on the variation of c-Si solar cell parameters under 8 MeV electron irradiation, *Sol. Energy Mater. Sol. Cells* 120 (2014) 191–196. doi:10.1016/j.solmat.2013.08.043.
- [11] S. Z. Karazhanov, Mechanism for the anomalous degradation of silicon space solar cells, *Applied Physics Letters* 76 (19) (2000) 2689–2691. doi:10.1063/1.126445.
- [12] O. Korotchenkov, H. Grimmliss, Long-wavelength acoustic-mode-enhanced electron emission from Se and Te donors in silicon, *Phys. Rev. B* 52 (20) (1995) 14598–14606. doi:10.1103/PhysRevB.52.14598.
- [13] S. S. Ostapenko, R. E. Bell, Ultrasound stimulated dissociation of Fe–B pairs in silicon, *J. Appl. Phys.* 77 (10) (1995) 5458–5460. doi:10.1063/1.359243.
- [14] O. Y. Olikh, The variation in activity of recombination centers in silicon p – n structures under the conditions of acoustic loading, *Semiconductors* 43 (6) (2009) 745–750. doi:10.1134/S1063782609060116.
- [15] D. Kropman, V. Seeman, S. Dolgov, A. Medvids, Effect of ultrasonic treatment on the defect structure of the Si–SiO₂ system, *phys. stat. sol. (c)* 13 (10–12) (2016) 793–797. doi:10.1002/pssc.201600052.

- [16] O. Y. Olikh, A. M. Gorb, R. G. Chupryna, O. V. Pristay-Fenenkov, Acousto-defect interaction in irradiated and non-irradiated silicon n^+-p structure, *J. Appl. Phys.* 123 (16) (2018) 161590. doi:10.1063/1.5001123.
- [17] Y. . Olikh, M. Tymochko, Reverse ultrasonic changes of electrical conductivity in CdTe:Cl crystals, *Superlattices Microstruct.* 95 (2016) 78–82. doi:10.1016/j.spmi.2016.04.038.
- [18] N. Zaveryukhina, E. Zaveryukhina, S. Vlasov, B. Zaveryukhin, Acoustostimulated changes in the density of surface states and their energy spectrum in p-type silicon single crystals, *Tech. Phys. Lett.* 34 (3) (2008) 241–243. doi:10.1134/S106378500803019X.
- [19] S. A. Mirsagatov, I. B. Sapaeva, Z. Nazarov, Ultrasonic annealing of surface states in the heterojunction of a $p\text{-Si}/n\text{-CdS}/n^+\text{-CdS}$ injection photodiode, *Inorganic Materials* 51 (1) (2015) 1–4. doi:10.1134/S0020168515010148.
- [20] S. Ostapenko, Defect passivation using ultrasound treatment: fundamentals and application, *Applied Physics A: Materials Science & Processing* 69 (2) (1999) 225–232. doi:10.1007/s003390050994.
- [21] I. Ostrovskii, O. Korotchenkov, O. Olikh, A. Podolyan, R. Chupryna, M. Torres-Cisneros, Acoustically driven optical phenomena in bulk and low-dimensional semiconductors, *J. Opt. A: Pure Appl. Opt.* 3 (4) (2001) S82–S86. doi:10.1088/1464-4258/3/4/364.
- [22] O. Y. Olikh, K. V. Voytenko, R. M. Burbelo, Ultrasound influence on I–V–T characteristics of silicon Schottky barrier structure, *J. Appl. Phys.* 117 (4) (2015) 044505. doi:10.1063/1.4906844.
- [23] O. Olikh, Features of dynamic acoustically induced modification of photovoltaic parameters of silicon solar cells, *Semiconductors* 45 (6) (2011) 798–804. doi:10.1134/S1063782611060170.
- [24] A. Davletova, S. Z. Karazhanov, A study of electrical properties of dislocation engineered Si processed by ultrasound, *Journal of Physics and Chemistry of Solids* 70 (6) (2009) 989–992. doi:10.1016/j.jpcs.2009.05.009.
- [25] A. Davletova, S. Z. Karazhanov, Open-circuit voltage decay transient in dislocation-engineered Si p–n junction, *Journal of Physics D: Applied Physics* 41 (16) (2008) 165107. doi:10.1088/0022-3727/41/16/165107.
- [26] V. Melnik, Y. Olikh, V. Popov, B. Romanyuk, Y. Goltvyanskii, A. Evtukh, Characteristics of silicon p–n junction formed by ion implantation with in situ ultrasound treatment, *Materials Science & Engineering, B: Solid-State Materials for Advanced Technology* 124–125 (2005) 327–330. doi:10.1016/j.mseb.2005.08.039.

- [27] O. Olikh, Reversible influence of ultrasound on γ -irradiated Mo/n-Si Schottky barrier structure, *Ultrasonics* 56 (2015) 545–550. doi:10.1016/j.ultras.2014.10.008.
- [28] A. Schenka, U. Krumbein, Coupled defect-level recombination: Theory and application to anomalous diode characteristics, *J. Appl. Phys.* 78 (5) (1995) 3185–3192. doi:10.1063/1.360007.
- [29] S. Steingrube, O. Breitenstein, K. Ramspeck, S. Glunz, A. Schenk, P. P. Altermatt, Explanation of commonly observed shunt currents in c-si solar cells by means of recombination statistics beyond the shockley-read-hall approximation, *J. Appl. Phys.* 110 (1) (2011) 014515. doi:10.1063/1.3607310.
- [30] V. Gopal, S. Gupta, Effect of dislocations on the zero-bias resistance-area product, quantum efficiency, and spectral response of LWIR HgCdTe photovoltaic detectors, *IEEE Trans. Electron Devices* 50 (5) (2003) 1220–1226. doi:10.1109/TED.2003.813230.
- [31] V. Gopal, S. Gupta, Contribution of dislocations to the zero-bias resistance-area product of LWIR HgCdTe photodiodes at low temperatures, *IEEE Trans. Electron Devices* 51 (7) (2004) 1078–1083. doi:10.1109/TED.2004.829857.
- [32] F. Mirzade, Elastic wave propagation in a solid layer with laser-induced point defects, *J. Appl. Phys.* 110 (6) (2011) 064906. doi:10.1063/1.3633524.
- [33] R. Peleshchak, O. Kuzyk, O. Dan’kiv, Formation of periodic structures under the influence of an acoustic wave in semiconductors with a two-component defect subsystem, *Ukr. J. Phys.* 61 (8) (2016) 741–746. doi:10.15407/ujpe61.08.0741.
- [34] A. B. Sproul, M. A. Green, Intrinsic carrier concentration and minority-carrier mobility of silicon from 77 to 300 K, *J. Appl. Phys.* 73 (3) (1993) 1214–1225. doi:10.1063/1.353288.
- [35] D. K. Schroder, *Semiconductor Material and Device Characterization*, 3rd Edition, John Wiley & Sons, New Jersey, 2006.
- [36] A. McEvoy, T. Markvart, L. Castaner (Eds.), *Solar Cells. Materials, Manufacture and Operation*, 2nd Edition, Academic Press, Oxford, 2013.
- [37] B. J. Hallam, M. D. Abbott, N. Nampalli, P. G. Hamer, S. R. Wenham, Implications of accelerated recombination–active defect complex formation for mitigating carrier-induced degradation in silicon, *IEEE Journal of Photovoltaics* 6 (1) (2016) 92–99. doi:10.1109/JPHOTOV.2015.2494691.
- [38] M. Razeghi, A. Rogalski, Semiconductor ultraviolet detectors, *J. Appl. Phys.* 79 (10) (1996) 7433–7473. doi:10.1063/1.362677.

- [39] J. Sun, Q. Zhang, E. P. Tsang, DE/EDA: A new evolutionary algorithm for global optimization, *Inform. Sci.* 169 (3–4) (2005) 249–262. doi:10.1016/j.ins.2004.06.009.
- [40] K. Wang, M. Ye, Parameter determination of Schottky–barrier diode model using differential evolution, *Solid-State Electron.* 53 (2) (2009) 234–240. doi:10.1016/j.sse.2008.11.010.
- [41] O. Y. Olikh, Review and test of methods for determination of the Schottky diode parameters, *J. Appl. Phys.* 118 (2) (2015) 024502. doi:10.1063/1.4926420.
- [42] K. Rühle, M. K. Juhl, M. D. Abbott, M. Kasemann, Evaluating crystalline silicon solar cells at low light intensities using intensity–dependent analysis of I–V parameters, *IEEE Journal of Photovoltaics* 5 (3) (2015) 926–931. doi:10.1109/JPHOTOV.2015.2395145.
- [43] N. Reich, W. van Sark, E. Alsema, R. Lof, R. Schropp, W. Sinke, W. Turkenburg, Crystalline silicon cell performance at low light intensities, *Sol. Energy Mater. Sol. Cells* 93 (9) (2009) 1471–1481. doi:10.1016/j.solmat.2009.03.018.
- [44] F. W. Chen, J. E. Cotter, M. D. Abbott, T.-T. A. Li, K. C. Fisher, The influence of parasitic effects on injection–level–dependent lifetime data, *IEEE Trans. Electron Devices* 54 (11) (2007) 2960–2968. doi:10.1109/TED.2007.906970.
- [45] O. Olikh, K. Voytenko, On the mechanism of ultrasonic loading effect in silicon–based Schottky diodes, *Ultrasonics* 66 (1) (2016) 1–3. doi:10.1016/j.ultras.2015.12.001.
- [46] D. Schroder, The concept of generation and recombination lifetimes in semiconductors, *IEEE Trans. Electron Devices* 29 (8) (1982) 1336–1338. doi:10.1109/T-ED.1982.20879.
- [47] H. Aharoni, T. Ohmi, M. M. Oka, A. Nakada, Y. Tamai, Analysis of n^+p silicon junctions with varying substrate doping concentrations made under ultraclean processing technology, *J. Appl. Phys.* 81 (3) (1997) 1270–1288. doi:10.1063/1.364442.
- [48] A. S. H. van der Heide, A. Schonecker, J. H. Bultman, W. C. Sinke, Explanation of high solar cell diode factors by nonuniform contact resistance, *Progress in Photovoltaics: Research and Applications* 13 (1) (2005) 3–16. doi:10.1002/pip.556.
- [49] J. Beier, B. Voss, Humps in dark I–V–curves — analysis and explanation, in: *Proceedings of the 23rd IEEE Photovoltaic Specialists Conference*, 1993, pp. 321–326, Louisville, KY, USA.

- [50] J. M. Shah, Y.-L. Li, T. Gessmann, E. F. Schubert, Experimental analysis and theoretical model for anomalously high ideality factors ($n \gg 2.0$) in AlGaIn/GaN p-n junction diodes, *J. Appl. Phys.* 94 (4) (2003) 2627–2630. doi:10.1063/1.1593218.
- [51] A. Kaminski, J. J. Marchand, H. E. Omari, A. Laugier, Q. N. Le, D. Sarti, Conduction processes in silicon solar cells, in: *Proceedings of the 25th IEEE Photovoltaic Specialists Conference*, 1996, pp. 573–576, Washington, DC, USA.
- [52] O. Breitenstein, J. Bauer, P. P. Altermatt, K. Ramspeck, Influence of defects on solar cell characteristics, *Solid State Phenomena* 156–158 (2010) 1–10. doi:10.4028/www.scientific.net/SSP.156-158.1.
- [53] D. G. Thomas, J. Hopfield, W. M. Augustyniak, Kinetics of radiative recombination at randomly distributed donors and acceptors, *Phys. Rev.* 140 (1A) (1965) A202–A220. doi:10.1103/PhysRev.140.A202.
- [54] O. Breitenstein, J. P. Rakotoniaina, M. H. Al Rifai, M. Werner, Shunt types in crystalline silicon solar cells, *Progress in Photovoltaics: Research and Applications* 12 (7) (2004) 529–538. doi:10.1002/pip.544.
- [55] V. Gopal, A new approach to investigate leakage current mechanisms in infrared photodiodes from illuminated current-voltage characteristics, *J. Appl. Phys.* 116 (8) (2014) 084502. doi:10.1063/1.4893899.
- [56] I. Baker, C. Maxey, Summary of HgCdTe 2D array technology in the U.K., *J. Electron. Mater.* 30 (6) (2001) 682–689. doi:10.1007/BF02665856.
- [57] N. Barth, R. Jovanovic, S. Ahzi, M. A. Khaleel, PV panel single and double diode models: Optimization of the parameters and temperature dependence, *Sol. Energy Mater. Sol. Cells* 148 (2016) 87–98. doi:10.1016/j.solmat.2015.09.003.
- [58] J. Evans-Freeman, D. Emiroglu, K. Vernon-Parry, J. Murphy, P. R. Wilshaw, High resolution deep level transient spectroscopy applied to extended defects in silicon, *J. Phys.: Condens. Matter.* 17 (22) (2005) S2219–S2227. doi:10.1088/0953-8984/17/22/009.
- [59] A. Castaldini, D. Cavalcoli, A. Cavallini, S. Pizzini, Experimental evidence of dislocation related shallow states in p-type Si, *Phys. Rev. Lett.* 95 (7) (2005) 076401. doi:10.1103/PhysRevLett.95.076401.
- [60] P. Omling, E. R. Weber, L. Montelius, H. Alexander, J. Michel, Electrical properties of dislocations and point defects in plastically deformed silicon, *Phys. Rev. B* 32 (10) (1985) 6571–6581. doi:10.1103/PhysRevB.32.6571.
- [61] M. Ogawa, S. Kamiya, H. Izumi, Y. Tokuda, Electronic properties of dislocations introduced mechanically at room temperature on a single crystal silicon surface, *Physica B: Physics of Condensed Matter* 407 (15) (2012) 3034–3037. doi:10.1016/j.physb.2011.09.139.

- [62] J. D. Murphy, K. Bothe, M. Olmo, V. V. Voronkov, R. J. Falster, The effect of oxide precipitates on minority carrier lifetime in p-type silicon, *J. Appl. Phys.* 110 (5) (2011) 053713. doi:10.1063/1.3632067.
- [63] M. Kim, M. Abbott, N. Nampalli, S. Wenham, B. Stefani, B. Hallam, Modulating the extent of fast and slow boron-oxygen related degradation in Czochralski silicon by thermal annealing: Evidence of a single defect, *J. Appl. Phys.* 121 (5) (2017) 053106. doi:10.1063/1.4975685.
- [64] K. Bothe, R. Sinton, J. Schmidt, Fundamental boron-oxygen-related carrier lifetime limit in mono- and multicrystalline silicon, *Progress in Photovoltaics: Research and Applications* 13 (4) (2005) 287–296. doi:10.1002/pip.586.
- [65] V. Vahanissi, A. Haarahiltunen, H. Talvitie, M. Yli-Koski, H. Savin, Impact of phosphorus gettering parameters and initial iron level on silicon solar cell properties, *Progress in Photovoltaics: Research and Applications* 21 (5) (2013) 1127–1135. doi:10.1002/pip.2215.
- [66] J. Schmidt, Effect of dissociation of iron-boron pairs in crystalline silicon on solar cell properties, *Progress in Photovoltaics: Research and Applications* 13 (4) (2005) 325–331. doi:10.1002/pip.594.
- [67] T. Mchedlidze, J. Weber, Iron-related carrier traps near the n^+p -junctions of crystalline silicon solar cells: impacts of feedstock and of the fabrication processes, *phys. stat. sol. (b)* 251 (8) (2014) 1608–1613. doi:10.1002/pssb.201451021.
- [68] T. Mchedlidze, L. Scheffler, J. Weber, M. Herms, J. Neusel, V. Osinniy, C. Moller, K. Lauer, Local detection of deep carrier traps in the pn-junction of silicon solar cells, *Appl. Phys. Lett.* 103 (01) (2013) 013901. doi:10.1063/1.4807142.
- [69] J. Murphy, J. McGuire, K. Bothe, V. Voronkov, R. Falster, Minority carrier lifetime in silicon photovoltaics: The effect of oxygen precipitation, *Sol. Energy Mater. Sol. Cells* 120 (2014) 402–411. doi:10.1016/j.solmat.2013.06.018.
- [70] J. Schön, A. Youssef, S. Park, L. E. Mundt, T. Niewelt, S. Mack, K. Nakajima, K. Morishita, R. Murai, M. A. Jensen, T. Buonassisi, M. C. Schubert, Identification of lifetime limiting defects by temperature- and injection-dependent photoluminescence imaging, *J. Appl. Phys.* 120 (10) (2016) 105703. doi:10.1063/1.4961465.
- [71] J. D. Murphy, K. Bothe, R. Krain, V. V. Voronkov, R. J. Falster, Parameterisation of injection-dependent lifetime measurements in semiconductors in terms of Shockley-Read-Hall statistics: An application to oxide precipitates in silicon, *J. Appl. Phys.* 111 (11) (2012) 113709. doi:10.1063/1.4725475.

- [72] L. Chen, X. Yu, P. Chen, P. Wang, X. Gu, J. Lu, D. Yang, Effect of oxygen precipitation on the performance of Czochralski silicon solar cells, *Sol. Energy Mater. Sol. Cells* 95 (11) (2011) 3148-3151. doi:10.1016/j.solmat.2011.06.044.